JVSTA Journal of Vacuum Science & Technology A

Effect of Sb thickness on the performance of bialkali-antimonide photocathodes

Md Abdullah A. Mamun, Abdelmageed A. Elmustafa, Carlos Hernandez-Garcia, Russell Mammei, and Matthew Poelker

Citation: Journal of Vacuum Science & Technology A **34**, 021509 (2016); doi: 10.1116/1.4939563
View online: http://dx.doi.org/10.1116/1.4939563
View Table of Contents: http://scitation.aip.org/content/avs/journal/jvsta/34/2?ver=pdfcov
Published by the AVS: Science & Technology of Materials, Interfaces, and Processing

Effect of Sb thickness on the performance of bialkali-antimonide photocathodes

Md Abdullah A. Mamun[a] and Abdelmageed A. Elmustafa
Department of Mechanical and Aerospace Engineering, Old Dominion University, Norfolk, Virginia 23529 and The Applied Research Center, Thomas Jefferson National Accelerator Facility, Newport News, Virginia 23606

Carlos Hernandez-Garcia, Russell Mammei, and Matthew Poelker
Thomas Jefferson National Accelerator Facility, Newport News, Virginia 23606

(Received 20 October 2015; accepted 23 December 2015; published 6 January 2016)

The alkali species Cs and K were codeposited using an effusion source, onto relatively thick layers of Sb (50 nm to ~7 μm) grown on GaAs and Ta substrates inside a vacuum chamber that was baked and not-vented, and also baked and vented with clean dry nitrogen but not rebaked. The characteristics of the Sb films, including sticking probability, surface roughness, grain size, and crystal properties were very different for these conditions, yet comparable values of photocathode yield [or quantum efficiency (QE)] at 284 V were obtained following codeposition of the alkali materials. Photocathodes manufactured with comparatively thick Sb layers exhibited the highest QE and the best 1/e lifetime. The authors speculate that the alkali codeposition enabled optimized stoichiometry for photocathodes manufactured using thick Sb layers, which could serve as a reservoir for the alkali materials. © *2016 American Vacuum Society*.
[http://dx.doi.org/10.1116/1.4939563]

I. INTRODUCTION

Among semiconducting photocathodes, the alkali-antimonides have attractive characteristics,[1–4] namely, high quantum efficiency (QE) and robust operation under relatively modest vacuum conditions, which makes them ideal for high current photogun[5–8] applications. The first successful demonstration of CsK_2Sb photocathodes in a normal conducting radio frequency gun was reported in the 1990s by Dowell *et al.*, which demonstrated QE of ~12% and then-record-level current production.[3] New light source initiatives,[9–11] proposed nuclear physics experiments such as DarkLight,[12] and electron cooling of proton beams for electron ion collider proposals[13,14] depend on high average current energy recovery linacs. These projects have generated renewed interest in alkali-antimonide photocathodes, which represent an excellent alternative to delicate negative electron affinity GaAs:Cs photocathodes,[15,16] providing similarly high QE but exhibiting less sensitivity to ion back bombardment and surviving under markedly harsher vacuum conditions.[3] Since alkali-antimonide photocathodes possess a positive-electron affinity, they are considered to be prompt emitters and therefore capable of producing shorter bunches, making them more attractive than the GaAs:Cs photocathodes for applications in high-brightness x-ray free electron lasers and fourth generation light sources.[2,7,17]

Photocathode performance relies on growth conditions defined by photocathode material composition, vacuum condition, and deposition process. Identifying optimum growth conditions for producing photocathodes that exhibit high QE and prolonged photocathode lifetime is of significant importance for the user-based accelerator applications listed above, and represents the main objective of this work. Photoguns typically employ front face illumination of the photocathode surface (not transmission mode), in which case, the thickness of the photocathode is not a limiting factor, at least not in terms of how the light is delivered. However, common recipes for alkali-antimonide fabrication rely on sequential deposition of K and Cs onto a relatively thin Sb layer (~15 nm)[18] similar to recipes used for photomultipliers tubes[19] where the Sb layer must transmit light. During photocathode fabrication, the chamber overall vacuum level and presence of water are known to affect the growth and morphology of Sb films.[20–23] To study the effect of these properties on the photocathode QE and lifetime, bialkali-antimonide photocathodes were successfully fabricated using an effusion source[24,25] by codeposition of Cs and K alkali species onto Sb layers of varying thickness. The Sb layer was grown simultaneously on GaAs and Ta substrates in a vacuum chamber following two distinct protocols: (1) photocathodes were prepared and evaluated in a vacuum chamber that was baked at 200 °C for 30 h each time the chamber was vented for loading new substrates (vent-bake protocol), and (2) photocathodes were prepared and evaluated in the same initially baked vacuum chamber, but the chamber was not baked again after venting with clean dry nitrogen when new substrates where installed (vent-no-bake protocol). Under these markedly different vacuum conditions, comparable QE values were obtained even though the Sb films exhibited very different growth characteristics. The highest measured QE values were ~10% at 532 nm. In contrast, the QE 1/e lifetime at low bias voltage showed a stronger dependence on the Sb layer thickness. In addition, this work demonstrates the practical advantages of using a relatively simple effusion source for codeposition of multiple alkali species, which appears to yield an optimized

[a]Electronic mail: mmamu001@odu.edu

stoichiometry in a straightforward manner, comparable to sequential deposition of individual alkali species. The present work provides a more detailed description of the experimental techniques previously reported by the authors[26] and adds surface science evaluation of Sb-film surface morphology, thickness, and structure by means of field emission scanning electron microscopy, x-ray diffraction, and atomic force microscopy.

II. EXPERIMENTAL DETAILS

This study was conducted in two phases: first, the Sb-film growth was characterized as a function of film thickness, and second, the Sb deposition processes of the first phase were repeated and followed by a codeposition of K and Cs to fabricate bialkali-antimonide photocathodes. Two groups of photocathodes were fabricated and evaluated for their QE and lifetime performance. Photocathodes within each group were distinct, having different Sb layer thickness, and with different surface morphology that resulted from the vent-bake and the vent-no-bake vacuum protocols. A detailed description of the complete apparatus and experimental techniques is presented below.

A. Deposition chamber

A dedicated vapor deposition chamber was designed, built, and commissioned for this study (Fig. 1). The bialkali-antimonide photocathodes were grown and evaluated at a low bias voltage of 284 V inside the vacuum chamber capable of operating in the UHV regime. The vacuum chamber, 20.3 cm in diameter and 38.1 cm long, was made from 304L stainless steel sheet, 0.48 cm thick with a 0.8 μm root mean square (RMS) surface finish that was rolled into a cylinder and welded. After manufacturing, the chamber was cleaned with a detergent[27] and solvents prior to assembly. The chamber included ports to accommodate pumps, a residual gas analyzer (RGA), source materials, the substrate holder with accompanying heater [Fig. 1(b)], a shutter to control chemical deposition onto the substrate, and view ports for sample illumination.

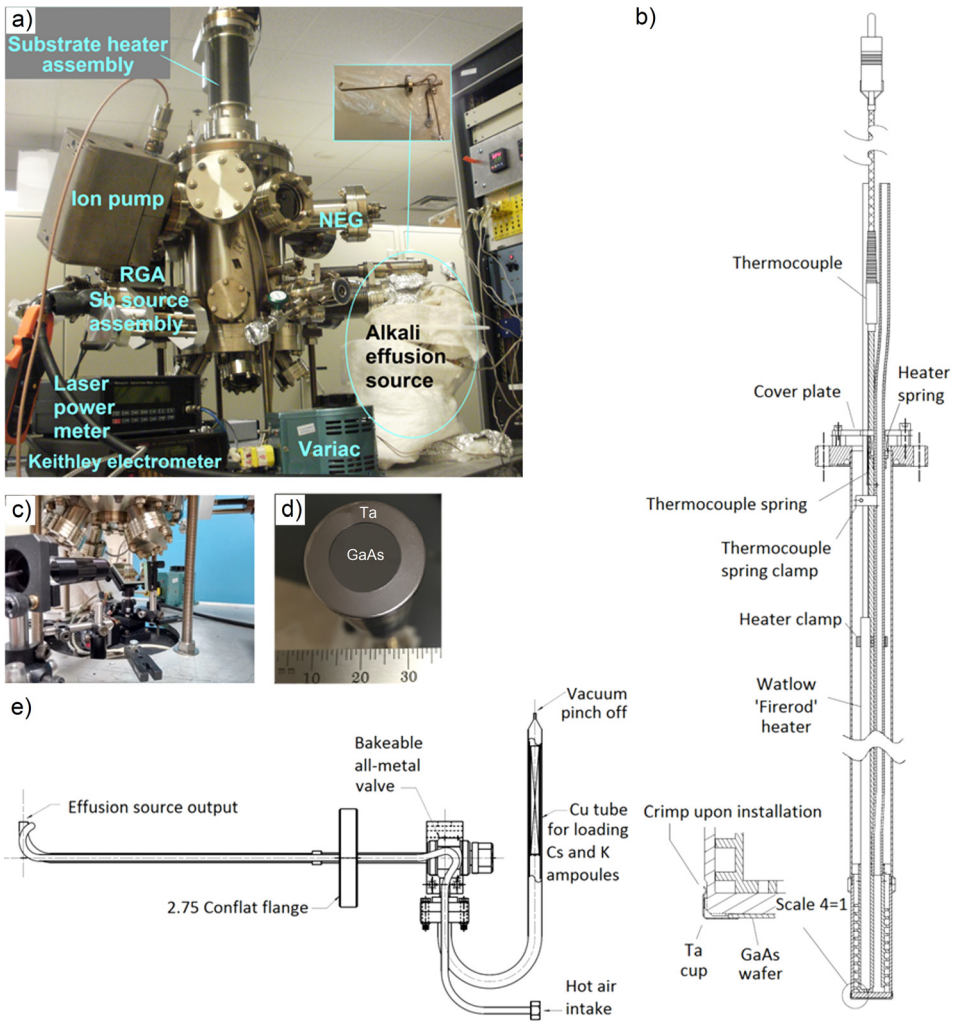

FIG. 1. (Color online) (a) Photograph of the bialkali-antimonide photocathode deposition chamber with effusion-type alkali dispenser (shown in the inset), (b) schematic of the substrate holder assembly with substrate heater, (c) photograph of the laser system with the mirrors attached to the stepper-motor-controlled translation stages, (d) photograph of the GaAs substrate secured to the sample holder using an annular Ta cup, and (e) schematic of the effusion-type alkali dispenser used for coevaporation of K and Cs species (with permission from Lawrence S. Cardman).

The vacuum was maintained using nonevaporable getter (NEG) pumps (two GP100 MK5 flange-mounted pumps and two WP950 NEG modules from SAES® Getters, with a total hydrogen pumping speed of 2780 l s^{-1}) and an ion pump (45 S Titan ion™ pump from Gamma vacuum, with a nitrogen pumping speed of ~401 s^{-1}). A turbomolecular pump was used to achieve a vacuum level suitable to energize the ion pump, and then valved out. The vacuum was continuously monitored using the ion pump current. The deposition chamber was equipped with an RGA mass spectrometer (SRS model RGA200) to continuously monitor the vacuum gas composition and it also served as a deposition monitor for the photocathode chemical species.[26] A single-side polished, p-doped, single-crystal GaAs (100) wafer of 0.5 mm thickness and 75 mm diameter was procured from AXT Company to use as substrate material. The Zn dopant concentration was in the range of $9.1(\pm 0.6) \times 10^{18}\,cm^{-3}$. The wafer was cleaved into square-shaped pieces, 1.5×1.5 cm, which could be attached to a 2 mm thick molybdenum disk brazed to the end of a long stainless steel tube that served as part of the vacuum enclosure. A heater with K-type thermocouple was inserted into the tubular substrate holder and pressed firmly against the back surface of the molybdenum disk (i.e., atmosphere side) via an applied spring force [Fig. 1(b)]. Calibration measurements indicated that the actual substrate temperature in vacuum was 80.8% that of the thermocouple reading. The GaAs substrate was secured to the sample holder using an unpolished annular Ta cup of 2.54 cm outer diameter (OD) that also served as a second substrate for the photocathode deposition [Fig. 1(d)]. A heater controller with feedback mechanism was used to control the substrate temperature. After heating, clean dry N_2 could be applied to the substrate holder (atmospheric side) to increase the substrate cooling rate. The substrate could be moved relative to the chemical sources via a bellows assembly with motorized drive screw. During chemical deposition, the substrate was maintained approximately 5 cm from the chemical sources.

The constituent sources consisted of high-purity (99.9999%) Sb pellets from Alfa Aesar,[28] and K (99.95% purity) and Cs (99.9+% purity) in 1 g breakseal ampoules from ESPI metals and Strem Chemicals, Inc., respectively. During deposition, the Sb pellets were resistively heated in a tungsten evaporation basket; whereas both alkali species were dispensed from a single effusion type reservoir [Fig. 1(e)]. The chamber was equipped with viewports made of Kodial Glass (alkali borosilicate 7056).

B. Vacuum protocols

During the course of this work, many Sb films and bialkali-antimonide photocathodes were fabricated. Initially, the entire apparatus was baked each time a substrate was replaced. Then, in the course of these studies, a small vacuum leak appeared in the deposition chamber. The leak was fixed but not before observing the fabrication of photocathodes with high QE under degraded vacuum conditions, with pressure roughly ten times higher than preleak conditions. This observation spurred the evaluation of Sb films and photocathodes under two different vacuum conditions designated as *vent-bake* and *vent-no-bake* protocols.

1. Vent-bake protocol

The evacuated chamber was baked for the first time at 200 °C for 180 h and leak checked with helium using the RGA (detectable leak threshold of 6.7×10^{-9} Pa l s^{-1}). At this point, the vacuum reached $\sim 6 \times 10^{-9}$ Pa; however, the vacuum degraded by approximately 1 order of magnitude following the breaking of alkali ampoules and heating of chemical sources. Each time a new substrate was installed, the apparatus was vented with clean dry N_2 from a large liquid nitrogen dewar and rebaked at 200 °C for 30 h. This vent-bake protocol consistently resulted in vacuum in the range of $\sim 10^{-7}$–10^{-8} Pa, with H_2 the dominant gas species, and lower levels of CH_4, CO, and CO_2. The partial pressure of water vapor was always less than 1% of the total pressure.

2. Vent-no-bake protocol

After repairing the small vacuum leak, Sb films and bialkali-antimonide photocathodes were fabricated without baking. Precautions were taken to minimize the amount of water vapor introduced to the system when venting including breaking only one flange joint at a time, and purging with a vigorous flow of clean dry N_2. While pumping the chamber with the turbomolecular pump, current was applied to the NEG pumps to degas them and restore pump speed. It was evident from the RGA spectrum that venting without further baking resulted in degraded vacuum, with pressure values now in the range of $\sim 10^{-6}$–10^{-7} Pa. The water vapor content increased by ~1 order of magnitude compared to the vent-bake protocol, although still representing near 1% of the total pressure. Moreover, water partial pressure reduced following each photocathode activation, which was likely a result of excess alkali deposited on the vacuum chamber walls serving as a getter.

For both vacuum protocols, the pressure within the chamber increased when the chemical sources were heated to operating temperatures. For the vent-bake condition, the chamber pressure during the bialkali deposition typically reached $> 5 \times 10^{-6}$ Pa but quickly improved to $\sim 10^{-7}$–10^{-8} Pa once the deposition ended. And for the vent-no-bake condition, the chamber pressure during the bialkali deposition typically reached $> 1 \times 10^{-5}$ Pa but quickly improved to $\sim 10^{-6}$–10^{-7} Pa once the deposition ended.

C. Antimony deposition and surface characterization

In preparation for Sb deposition, the substrate was moved away from the chemical sources and heat cleaned at 550 °C for 2 h. A shutter mechanism, placed at few centimeter in front of the substrate, prevented contamination of the chemical sources and of the viewport used for transmitting light to the photocathode. At the end of heat cleaning and immediately prior to Sb deposition, the substrate was rapidly cooled to 200 °C and kept behind the shutter while resistive heating of the Sb crucible was initiated. Antimony was evaporated

from an aluminum oxide crucible that was resistively heated by applying current to a tungsten wire basket that supported the crucible, from a regulated DC power supply (Electronic Measurements, Inc., TCR 40S45–1D-OV DC power supply 0–40 V, 0–45 A, 1800 W). The crucible with tungsten evaporation basket was initially loaded with approximately 1 g of high-purity (99.9999%) Sb pellets. The Sb partial pressure detected by the RGA was constantly monitored. The current applied to the tungsten heater was varied to obtain the desired partial pressure of Sb at which point the shutter was retracted and the substrate was lowered from the parking position to a working distance of 5 cm from the source. To obtain a variety of Sb film thicknesses, the current applied to the Sb heater basket was varied from 31.2 to 33.7 A and the deposition time was varied from 30 to 120 min. Under these conditions, the partial pressure of the Sb vapor varied from $7.3(\pm 0.6) \times 10^{-9}$ to $1.3(\pm 0.3) \times 10^{-8}$ Pa. After Sb deposition, the electrical current applied to the tungsten crucible heater was terminated and the Sb source was retracted to a parking position behind a fixed shutter. At this point, the temperature of the substrate was decreased to 120 °C for alkali deposition, or to room temperature for Sb film characterization.

The Sb film thickness values were determined by repeatedly growing Sb films on the GaAs and Ta substrates inside the deposition chamber. After growing a Sb film, the substrates were removed from the chamber and evaluated using the surface science tools listed below, to determine grain structure, morphology, surface roughness, and porosity as a function of Sb thickness. All of these characteristics represent important metrics that could help improve our understanding of the role of the Sb layer on photocathode performance. For Sb film characterization, no alkali species were evaporated onto the substrates.

The film thickness and surface topography were investigated using a cold emission type high resolution Hitachi S-4700 field emission scanning electron microscope (FESEM), and a JEOL JSM-6060 LV scanning electron microscope (SEM). The SEM was operated at an accelerating voltage of 30 kV with a working distance of 10 mm, while the FESEM was operated at an accelerating voltage of 15 kV with a working distance of ~12 mm, resulting in a spatial resolution of up to 1.5 nm. The cross-section FESEM imaging was performed for film thickness evaluation. A Bruker-AXS (Bruker AXS, Inc., Madison, WI) three circle diffractometer equipped with a SMART Apex II CCD detector and graphite monochromated Cu-K_α radiation source was used for x-ray diffraction (XRD) measurements, to study film structure. The films were identified in the symmetric $\theta/2\theta$ geometry, ranging from $2\theta = 20°$ to 70°. The surface roughness of the films was examined in tapping mode using a Digital Instruments Dimension 3100 atomic force microscope (AFM) from Veeco.

D. Effusion source for alkali codeposition

As mentioned previously, many traditional procedures for alkali-antimonide photocathode fabrication employ sequential deposition of K and Cs on a ~15 nm Sb film. However, for photocathodes with a thicker Sb layer, we suggest that codeposition of alkali species provides a more optimized stoichiometry. Our photocathodes[26] were fabricated by codeposition of both alkali species using the effusion source depicted in Fig. 1(e). The so-called effusion source was a common device used on dc high voltage photoguns from the 1970s through the 1990s, to fabricate CsO-GaAs photocathodes that possess a negative electron affinity.[29] The effusion source was eventually replaced by the now widely used Cs_2CrO_4 based alkali source[30] for GaAs photocathode applications, in large part because they are easier to use. However, for alkali-antimonide photocathode fabrication, the effusion source offers advantages over other alkali sources. Namely, it is a comparatively high capacity source that readily supports codeposition of multiple alkali species. It is also relatively compact, with a small control valve that can be closed to preserve the alkali supply when the rest of the vacuum system is vented. Or conversely, the control valve can be closed to allow alkali replacement without venting the rest of the deposition chamber.

For charging the effusion dispenser with alkali species, 1 g breakseal ampoules of K (1 cm OD) and Cs (0.6 cm OD) under argon atmosphere were inserted into the 1.27 cm OD (1.12 cm inner diameter) copper pinch-off tube (CPT-133–050 from Huntington Mechanics Lab) with a 1.33 in. mini-Conflat flange on one side that was attached to the control valve of the effusion dispenser. The copper tube thus served as the alkali reservoir of the effusion dispenser. The open end of the copper tube was pinched-off, to make a vacuum tight seal and heated to desorb water while evacuated through the valve. The glass ampoules were then broken by slightly pinching the outside of the copper tube, cracking the glass ampoules and thus liberating the argon gas which was pumped away. This alkali charging of effusion dispenser was done during the chamber assembly phase and provided enough source chemicals for all the activations performed for this study, and many others not included in this summary. To evaporate alkali metals during photocathode fabrication, hot air was passed through the heating tube that represents a central design feature of the effusion source, with the control valve open. The alkali temperature was kept constant by electrical feedback applied to the hot air source. To terminate the flow of alkali, one simply closed the control valve and retracted the effusion source behind a fixed shield that blocked the line of sight to the substrate.

E. Photocathode preparation

Photocathodes were fabricated using a two-step deposition scheme: Sb was first deposited onto substrates maintained at 200 °C, followed by codeposition of alkali species with the substrate at 120 °C and falling to 80 °C during the course of photocathode fabrication. Reducing the temperature of the substrate during alkali deposition helped to optimize QE, by providing more control over the photocurrent rate of rise. Alkali deposition was terminated when the photoemission current reached a maximum. When not in use,

the effusion source was retracted beneath the shutter with control valve closed. After photocathode fabrication, the substrate was cooled to room temperature passively or more quickly using a nitrogen purge. It is possible to prepare photocathodes on substrates maintained at room temperature; however, evaporation on a heated substrate enhances diffusion of the alkali materials into the bulk material,[31] which becomes critical for thick alkali-antimonide photocathode formation.

Details of Sb evaporation were described in Sec. II C. Immediately prior to alkali deposition, the substrate temperature was brought to 120 °C, and the substrate was placed in the parking position behind the shutter. At this point, the preheated effusion source was moved to the center of the chamber and the control valve was then slightly opened. Evaporation of combined alkali species was controlled by adjusting the heater power and the hot air flow rate applied to the effusion source, and by regulating the control valve. Fine tuning the temperature distribution of different parts of the effusion source was achieved through judicious application of thermal insulation. Additional heat could be applied to the reservoir tube using an independently controlled heat tape to increase the alkali flux when required. The partial pressure of the alkali vapors was constantly monitored by the RGA. When the desired partial pressure of alkali was achieved, the substrate shutter was retracted, and the substrate was lowered from the parking position to the deposition plane at a distance of 5 cm from the source plane. The different parts of the effusion source were maintained at stable temperatures during alkali evaporation. To adjust the alkali deposition rate for different photocathodes, these temperatures were varied over the following ranges: the hot air inlet tube (381–462 °C), the dispensing tube (232–294 °C), and the reservoir tube (153–281 °C). The partial pressure of the alkali vapors was recorded during deposition. As an example, for 387 °C at the inlet tube, 259 °C at the dispensing tube, and 184 °C at the reservoir, the partial pressure for Cs and K was recorded as $1.8(\pm 0.10) \times 10^{-8}$ and $4.2(\pm 0.50) \times 10^{-9}$ Pa, respectively.

F. Photoemission characterization

During application of alkali species, the electrically grounded substrate and Sb film were illuminated with 4 mW of green light (532 nm) from a temperature stabilized laser with 284 V applied to a nearby anode ring. The anode ring was electrically isolated from ground and attached to a sensitive current meter (Keithley electrometer model 617) to detect the photocurrent. The laser power was never attenuated, and no attempt was made to limit the extracted photocurrent, which for the best photocathodes could reach 200 μA. Following fabrication, the photocathode performance was assessed by measuring QE and QE 1/e lifetime at 532 nm. The QE represents a fraction of the incoming photons that produce photoemitted electrons and can be calculated using the equation[32]

$$\mathrm{QE}(\%) = \frac{Ihc}{\lambda eP} \times 100\% = \frac{124I}{\lambda P}, \quad (1)$$

where P (mW) is laser power, I (μA) is the measured photocurrent, λ is the laser wavelength (nm), h is Planck's constant (6.626×10^{-34} J s), e is the electron charge (1.6×10^{-19} C), and c is the velocity of light (2.998×10^{8} m s^{-1}).

In order to map the QE across the photocathode surface, the laser beam could be moved across the substrate using mirrors attached to the stepper-motor-controlled translation stages [Fig. 1(c)]. The QE measurements were repeated at different time intervals to evaluate photocathode QE lifetime, a metric describing the length of time required to observe QE decay to 1/e of its initial value. The QE lifetime was determined using a least square fit to the QE decay trend. To map the photocathode spectral response over a broad wavelength range from 425 to 825 nm, the simple low power 532 nm laser was replaced with a wavelength tunable white-light supercontinuum laser.[33] During this measurement, a calibrated Si photodiode power meter was used to measure the incident laser power at each wavelength.

III. RESULTS AND DISCUSSION

A. Effect of vacuum practice on Sb growth

Surface science evaluation of the Sb layers deposited on Ta and GaAs substrates, using different vacuum protocols and deposition conditions, provided morphological and structural information as a function of Sb thickness. FESEM, XRD, and AFM results discussed in this section represent important metrics to improve our understanding of the role of Sb layers on photocathode performance.

1. FESEM results

Variations in deposition time, deposition rate (set by the current applied to the Sb crucible heater, and monitored via the Sb partial pressure with the RGA), and vacuum protocols had a significant impact on Sb-film growth on GaAs and Ta substrates. Figure 2 shows FESEM-generated images of surface topography and cross-section views of Sb layers on Ta and GaAs substrates for two different Sb deposition time intervals and partial pressures [100 and 120 min, $7.33(\pm 0.6) \times 10^{-9}$ and $1.33(\pm 0.3) \times 10^{-8}$ Pa, respectively] for two different vacuum protocols (vent-bake and vent-no-bake). The right-most column of Fig. 2 shows Sb-film cross-sectional views obtained by cleaving the GaAs wafer substrate using a diamond-tipped scribe. It was not possible to cleave the Ta substrate to obtain such cross-sectional views. The Sb grain size and film thickness increased dramatically with increasing the deposition time and deposition rate. The Sb film thickness, defined as the distance from the substrate to the outermost edge of the Sb grains, was measured in the range of 50 nm to ~6.7 μm from the GaAs substrates. In general, grain size and porosity of the Sb films increased significantly with increasing film thickness.

It is evident from Fig. 2(a) that Sb growth occurred more favorably on the Ta substrate for the vent-bake protocol at a reduced deposition rate. Under these conditions, granular Sb

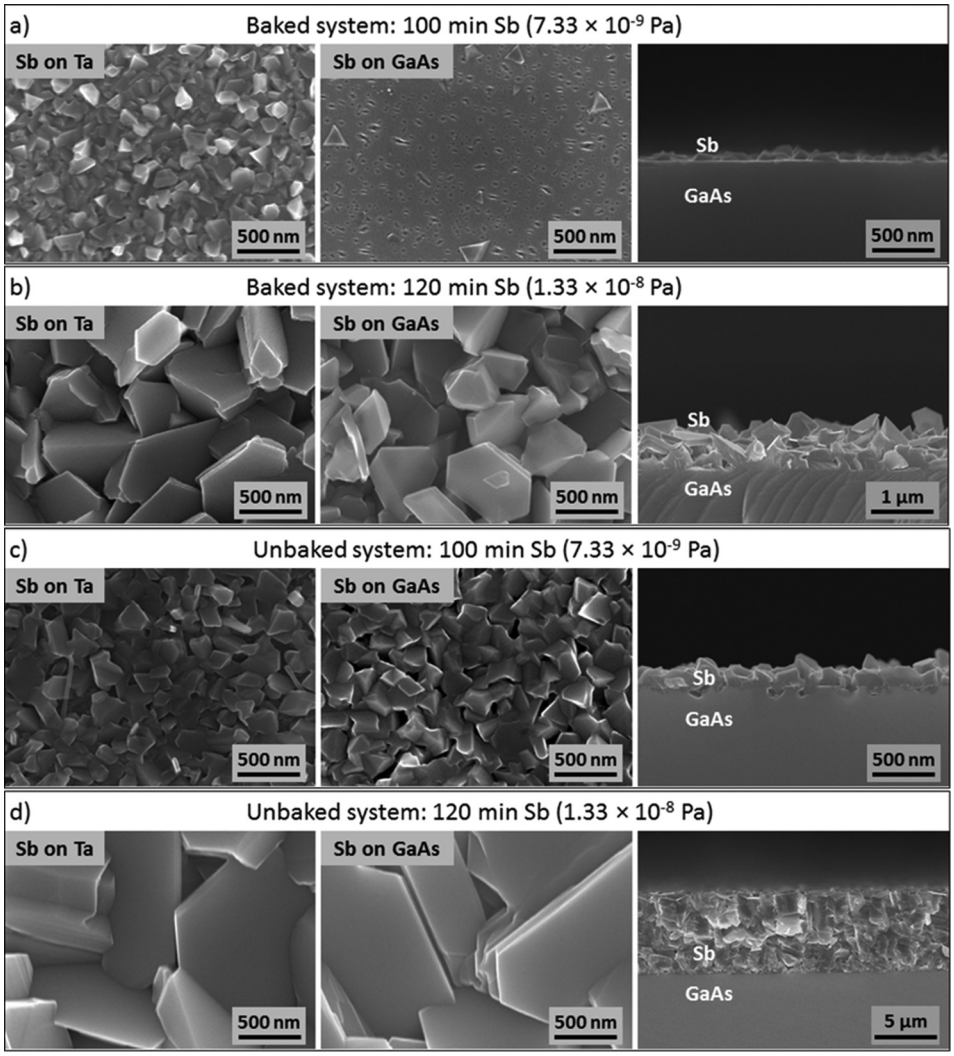

FIG. 2. FESEM images illustrating topography and cross-sectional views of Sb films grown on Ta and GaAs substrates for 100 and 120 min deposition times, with 32.7(±0.2) and 33.7(±0.2) A current, respectively, applied to the Sb crucible heater, under two different vacuum protocols: [(a) and (b)] vent-bake and [(c) and (d)] vent-no bake. For vent-bake vacuum protocol, the normal operating pressure was $\sim 10^{-7}$ Pa. For vent-no bake vacuum protocol, the pressure was $\sim 10^{-6}$ Pa.

structure was observed on the Ta substrate whereas Sb grain nucleation was prevalent for the GaAs substrate. As the deposition rate and duration was increased, both substrates depicted granular and porous Sb film structure with similar large grains [Fig. 2(b)].

In contrast, for the vent-no-bake protocol, the overall growth of Sb was favored equally on both substrates irrespective of the Sb deposition rate [Figs. 2(c) and 2(d)]. Moreover, a noticeable increase in grain size and Sb thickness was also observed compared to the vent-bake protocol, which resulted in an enhancement of the grain size and the thickness by factors of ~2 and 7, respectively. Once an initial monolayer of Sb is formed, a subsequent Sb growth can be expected to take place at a similar rate. The grain size and the variations in Sb film thickness on GaAs and Ta substrates became minimized once the Sb film grew thicker.

2. XRD results

X-ray diffraction is a common technique used to study the crystal structure of materials. The crystal structure and the average crystallite size of the Sb films were studied using x-ray powder diffraction. Figure 3 shows the XRD patterns of the Sb thin films deposited on GaAs(1 0 0) substrates for 2θ range of 20°–70°. The Sb films exhibited an amorphous structure when very thin, and developed into trigonal[34] and hexagonal[35] polycrystalline phases as they grew thicker. The hexagonal phases are identified in crystallographic planes (1 0 0) and (2 0 0). Similar to the observations reported by Liang *et al.*,[36] the diffraction peaks for the Sb films appeared to change as the film thickness and evaporation rate changed. With the emergence of increasing number of nucleation sites as the film thickness increased, the Sb film transitioned from amorphous to crystalline structure. During this transition, the dominant crystallographic plane changed from (2 0 0) to (1 1 6) as indicated by the Sb films with thickness 0.06 and 0.12 μm. A similar change was observed from the thickest Sb film (6.7 μm) where Sb deposition was performed at a higher Sb evaporation rate (by a factor of ~1.9). This was indicated by the emergence of (1 0 4) as the dominant crystallographic plane. The dominant crystallographic planes were identified as (2 0 0), (1 1 6), (1 1 6), (1 1 6), (1 1 6),

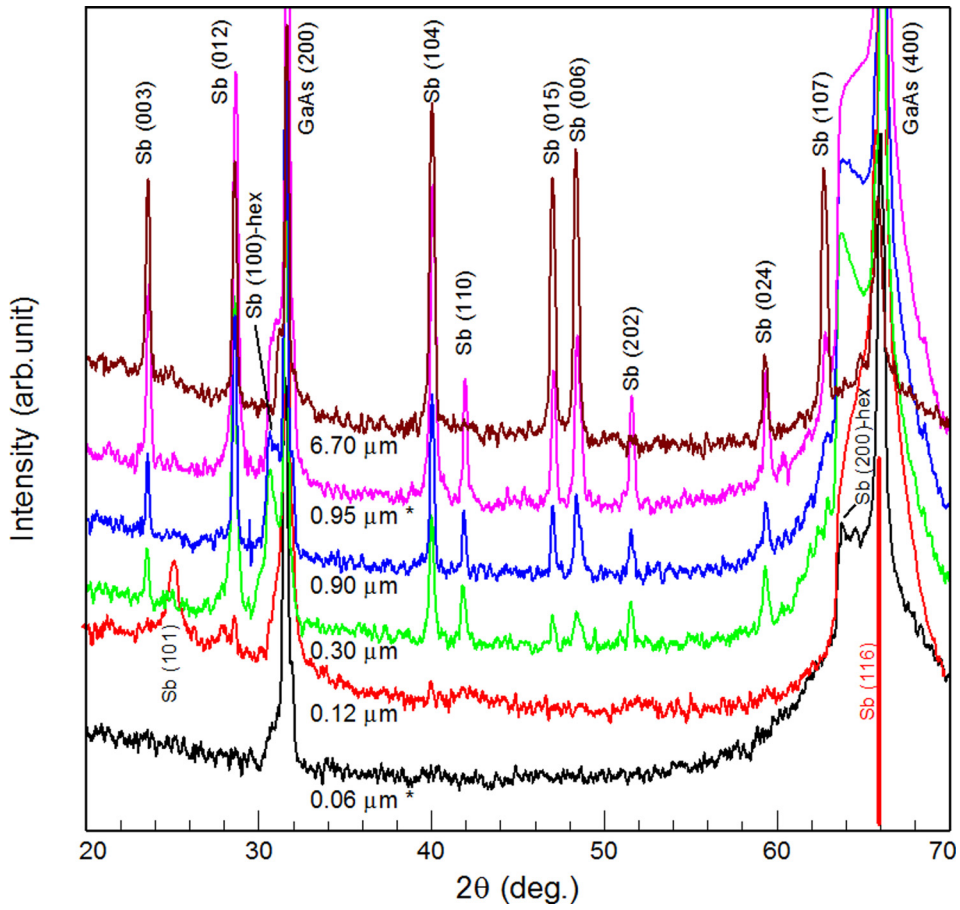

FIG. 3. (Color online) XRD patterns of Sb films with varying thicknesses deposited on GaAs substrate. Antimony films deposited under vent-bake protocol are labeled with asterisk (*).

and (1 0 4) for films with thickness 0.06, 0.12, 0.3, 0.9, 0.95, and 6.7 μm, respectively. The average crystallite sizes of the Sb films were estimated from the dominant peaks using Debye-Scherrer formula[37]

$$D = \frac{K\lambda}{\beta(2\theta)\cos\theta}, \tag{2}$$

where D is the mean crystallite size, K is the shape factor, λ is the x-ray wavelength ($\lambda = 1.54$ Å for Cu-K_α radiation), $\beta(2\theta)$ is the full width at half maximum (FWHM), and θ is the Bragg angle. The FWHM of the dominant crystallographic planes was evaluated as 2484, 1617, 1749, 1677, 1794, and 565 arc sec for 0.06, 0.12, 0.3, 0.9, 0.95, and 6.7 μm Sb films, respectively. The corresponding mean crystallite sizes were evaluated as 13.57, 21.12, 19.47, 20.31, 19.01, and 53.92 nm for the determined dominant planes (2 0 0), (1 1 6), (1 1 6), (1 1 6), (1 1 6), and (1 0 4). These values indicate that the crystallite sizes of ~13.6, 20.0, and 53.9 nm are dependent on the crystallographic planes (2 0 0), (1 1 6), and (1 0 4). In thin films, crystallite size may affect the microstructural and electrical properties.[38] The increased crystallite size often indicates a decreased level of residual stress and defect density[39] that can result in lowering film resistivity due to reduced grain boundary scattering.

3. AFM results

AFM images illustrated in Fig. 4 represent the surface morphology of the Sb films grown on Ta and GaAs substrates using the vent-no-bake protocol. The RMS roughness measured over a $10 \times 10\,\mu m^2$ area of the Sb film increased from 122 to 157 nm on the Ta substrate, and from 42 to 130 nm on the GaAs substrate for the deposition rate and durations of 7.33×10^{-9} to 1.33×10^{-8} Pa and 100 to 120 min, respectively. Under these conditions, the size of the largest Sb grains varied similarly on both substrates, with Sb grain size increasing from 0.6 to 2.6 μm, as measured by the AFM section analysis.

The AFM-measured roughness and maximum grain size of the Sb films grown on GaAs substrate was plotted versus FESEM-measured Sb film thickness, as shown in Fig. 5. The Sb grain-size enlargement exhibited a power scaling relationship with the Sb thickness and was not influenced by the evaporation rate of Sb. In contrast, the RMS roughness demonstrated a great influence by the evaporation rate of Sb in addition to the Sb film thickness. This was evidenced by the increasing trend of Sb surface roughness with the Sb thickness and grain size, which ceased when the evaporation rate of Sb was increased by a factor of ~1.9, resulting in a horizontal tail in the graph. This observation reinforces the conclusion made by Liang *et al.*[36] that a high deposition rate

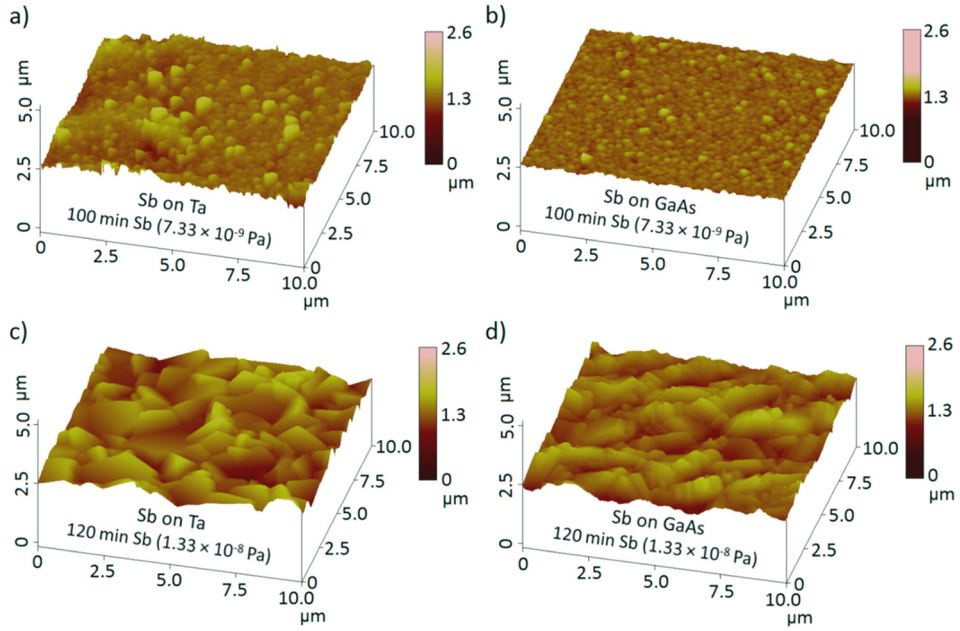

FIG. 4. (Color online) AFM images illustrating surface morphology of Sb films grown on Ta and GaAs substrates for [(a) and (b)] 100 min with 32.7(±0.2) A, and [(c) and (d)] 120 min with 33.7(±0.2) A current applied to the Sb crucible heater following the vent-no bake protocol.

of Sb is desirable to avoid a high roughness surface. The least square fit of all-inclusive roughness data resulted in an asymptotic relationship. Assuming similar relationships for Sb films grown on Ta substrates, the grain size and roughness fits were used to estimate Sb film thickness on Ta substrates (Table I), where FESEM cross-sectional views were not possible to obtain.

B. Quantum efficiency of photocathodes

Literature suggests that the QE of alkali-antimonide photocathodes is highly sensitive to the stoichiometry of the constituent elements.[40] During photocathode fabrication, both substrates were simultaneously exposed to the same amount of evaporated sources, but as the alkali species were deposited subsequent to the Sb deposition, any difference in the Sb layer thickness or morphology on each substrate could lead to dissimilar stoichiometry and QE distribution.

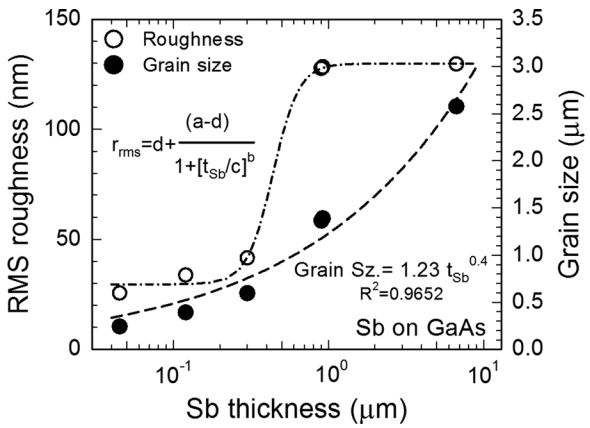

FIG. 5. RMS roughness and grain size as function of Sb thickness for Sb films deposited on GaAs substrate. Fitting parameters: a = 29.57444, b = 5.248599, c = 0.4383123, and d = 129.843 (R^2 = 0.9976).

Prior to QE evaluation, photocathodes were cooled to room temperature, and the QE was allowed to stabilize for 6 to 12 h. During this time, it was presumed that excess Cs slowly desorbed from the photocathode surface due to the high vapor pressure even at room temperature. Moreover, the effect of superficial oxidation occurred during this time could significantly enhance the quantum yield of this photocathode.[41] The stabilized QE of each photocathode was then mapped across the entire photocathode surface using the low power green laser, with <1 mm diameter spot size (FWHM), rastered in steps of ~0.5 mm.

QE maps illustrating key observations are shown in Fig. 6. The QE maps obtained via the vent-bake protocol [Figs. 6(a) and 6(b)] indicate that QE could be optimized on one substrate or the other, but not on both simultaneously. In contrast, the QE map obtained via the vent-no-bake protocol [Fig. 6(c)] shows relatively uniform QE across both substrates. To facilitate the discussion, representative FESEM topography images and relevant QE maps are shown in Fig. 7. It is not surprising to see markedly different QE on the GaAs and Ta substrates because Sb growth was favored on the Ta substrate using the vent-bake protocol [Fig. 7(a)]. Although relatively high QE could be achieved on both substrates, the chemical deposition conditions for the resulting optimized QE were markedly different. In this case, the photocathode on the GaAs substrate was optimized for the QE whereas the Ta substrate exhibited no QE because the deposited alkali materials did not reach a critical level to produce optimized stoichiometry of the photocathode on the relatively thicker Sb layer. For the vent-no-bake condition, which supported the Sb film growth equally on both substrates, the QE maps were more uniform across both substrates [Fig. 7(b)].

Optimized QE values for each substrate as a function of the Sb film thickness are illustrated in Fig. 8, where film

TABLE I. List of deposition conditions and the corresponding Sb thickness in micrometer. On GaAs substrates, a direct measurement of Sb film thickness was possible via cross-section views using FESEM. For Ta substrates, the Sb film thickness was estimated using the relationship obtained among grain size, roughness, and thickness from Sb films on GaAs.

		Sb thickness (μm)			
		Vent-bake		Vent-no bake	
Deposition time (min)	Partial pressure of Sb in RGA detector (Pa)	GaAs	Ta	GaAs	Ta
30	$7.3(\pm0.6)\times10^{-9}$	—	0.03[a]	0.045[a]	0.06[a]
70	$7.3(\pm0.6)\times10^{-9}$	0.06	—	0.12	0.18[a]
100	$7.3(\pm0.6)\times10^{-9}$	0.10	0.245[a]	0.30	0.31[a]
120	$7.0(\pm0.6)\times10^{-9}$	—	—	0.90	0.92[a]
120	$1.3(\pm0.3)\times10^{-8}$	0.95	1.15[a]	6.70	7.27[a]

[a]Estimated values.

thickness values represent estimates based on the surface science results described above. The QE values varied from ~3% to 10% for photocathodes with Sb layer thickness from <50 nm to ~7 μm. Recent literature reports that crystallinity of the Sb film can influence the photocathode sensitivity[42] and that a variation in crystallite sizes can affect the energy bandgap.[43] These observations can explain the trend toward higher QE for thicker Sb films, namely, thicker films resulted in increased average crystallite and grain size, which could serve to reduce the energy band gap of the photocathodes.

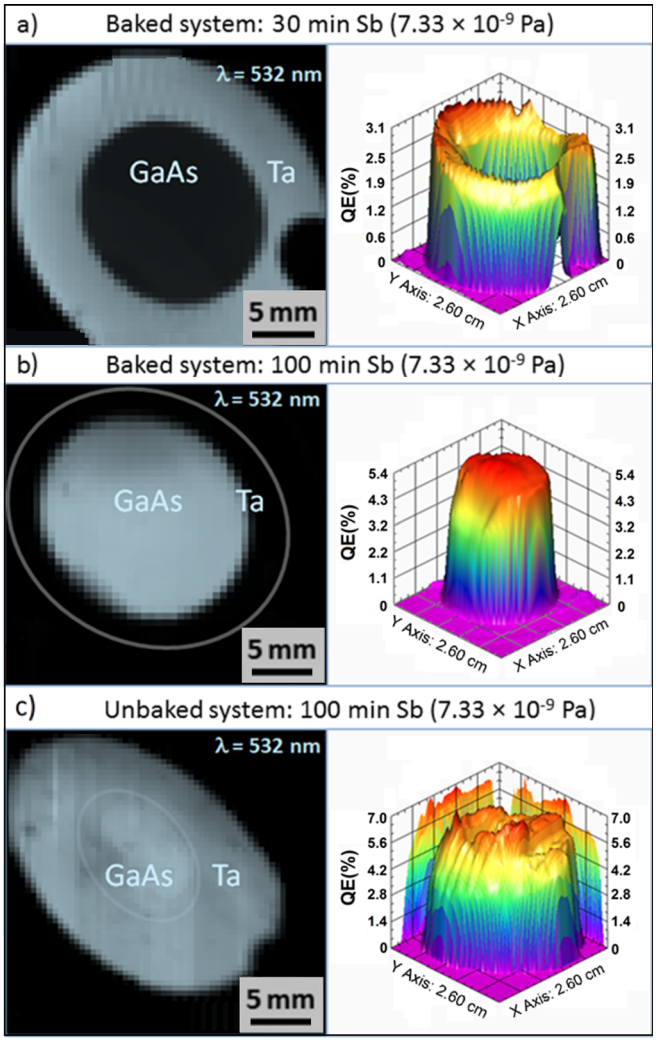

FIG. 6. (Color online) QE (%) map of the photocathodes biased at 284 V with 532 nm (3.96 mW). The photocathodes were prepared by bialkali codeposition following the vent-bake protocol on (a) a 30 min grown Sb layer and (b) a 100 min grown Sb layer; and following the vent-no bake protocol on (c) a 100 min grown Sb layer. Z axis in the 3D plot represents QE (%).

Others report QE of 10% and higher[3,44] for bialkali-antimonide photocathodes fabricated with very thin Sb layers (~15 nm), whereas our measured values were considerably lower for thin photocathodes. It is possible that for thin photocathodes, greater care must be taken when preparing the substrates. For example, typical alkali-antimonide photocathode recipes employing silicon substrates rely on the removal of native oxides via acid etching prior to the installation of the substrates within the deposition chamber.[45] It is well established that in order to remove oxide and carbon contamination from the substrate surface, atomic hydrogen cleaning effectively improved the QE in GaAs:Cs photocathodes.[46] In this work, the GaAs substrates were removed from the vendor shipping containers, cleaved to size and then installed inside the deposition chamber without any further preparation. The Ta substrates were cleaned in an ultrasonic bath of acetone, followed by methanol, and then installed. Once inside the vacuum chamber, the substrates were routinely heated to 550 °C for 2 h prior to photocathode fabrication, which served to liberate weakly bound gas and contamination but could not effectively remove the native oxides.

It was relatively easy to obtain more QE data points following the vent-no-bake protocol as compared to the vent-bake protocol because the Sb growth was equally favored on both substrates and hence resulted in a similar Sb structure and morphology. This resulted in optimal photocathode stoichiometry on both Ta and GaAs substrates simultaneously, for any Sb thickness. It was more challenging to obtain a full data set for the vent-bake vacuum protocol because the vent-bake condition provided dissimilar Sb films which made it difficult to optimize the QE on each substrate.

C. QE lifetime of photocathodes

The QE lifetime was evaluated for photocathodes manufactured under the vent-no bake protocol, by continuous illumination of photocathodes at a single location on each

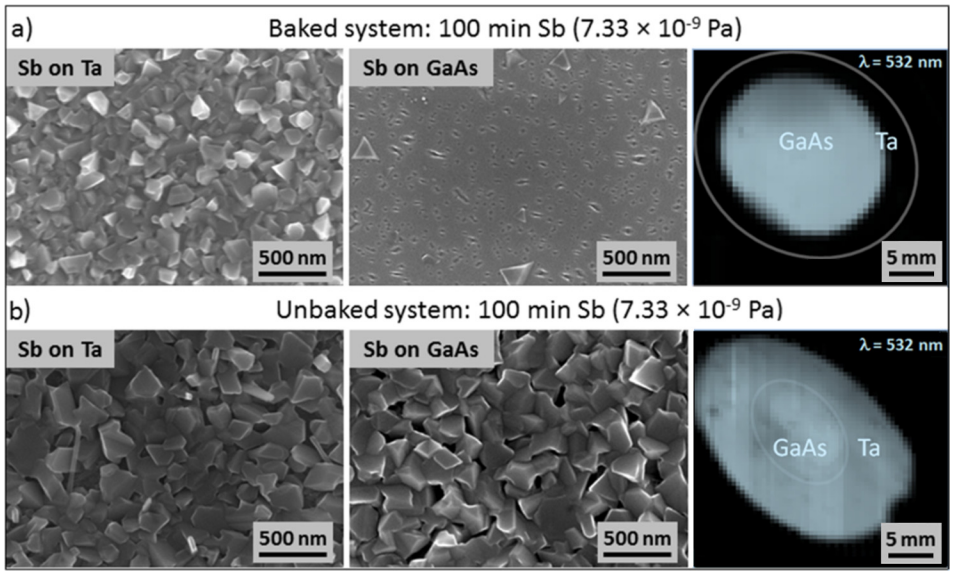

FIG. 7. (Color online) FESEM topography and QE distribution of the photocathodes biased at 284 V with 532 nm (3.96 mW). The photocathodes were prepared by bialkali codeposition following the (a) vent-bake protocol on a 100 min grown Sb layer and (b) vent-no bake protocol on a 100 min grown Sb layer.

substrate, for an extended time period. All of the photocathodes depicted a decaying QE with time, but at different rates [Fig. 9(a)]. During electron beam extraction from a photocathode under high bias voltage, QE decay is caused by different mechanisms such as ion bombardment and chemical poisoning of the activated photocathode surface.[15] Since our experiments were conducted at low voltage, chemical poisoning is likely to be the dominant mechanism to impact lifetime. The QE 1/e lifetimes obtained from the least square fit of the QE decay data are illustrated as a function of Sb thickness in Fig. 9(b). The QE lifetime for photocathodes grown on the GaAs substrate exhibited a power-law dependence on the Sb film thickness. The photocathode with the thickest Sb film (6.7 μm) provided the longest lifetime ($\sim$42 days). However, the lifetime results for photocathodes grown on the Ta substrates are inconclusive. The photocathode with a 300 nm Sb film provided stable photocurrent at 200 μA for over 5 days. A photocurrent decay was experienced

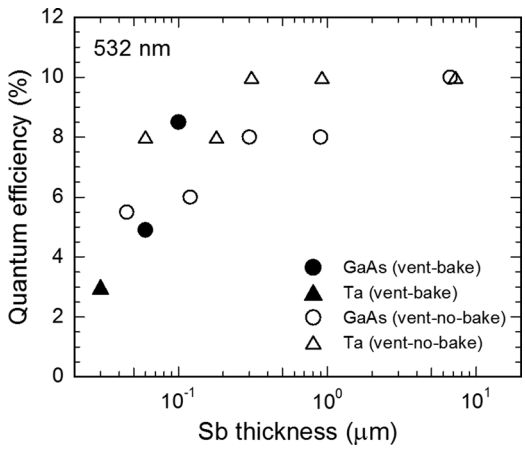

FIG. 8. QE as a function of Sb thickness for bialkali-antimonide photocathodes deposited on Ta and GaAs substrates. The photocathodes were biased at 284 V and illuminated with 4 mW of laser light at 532 nm.

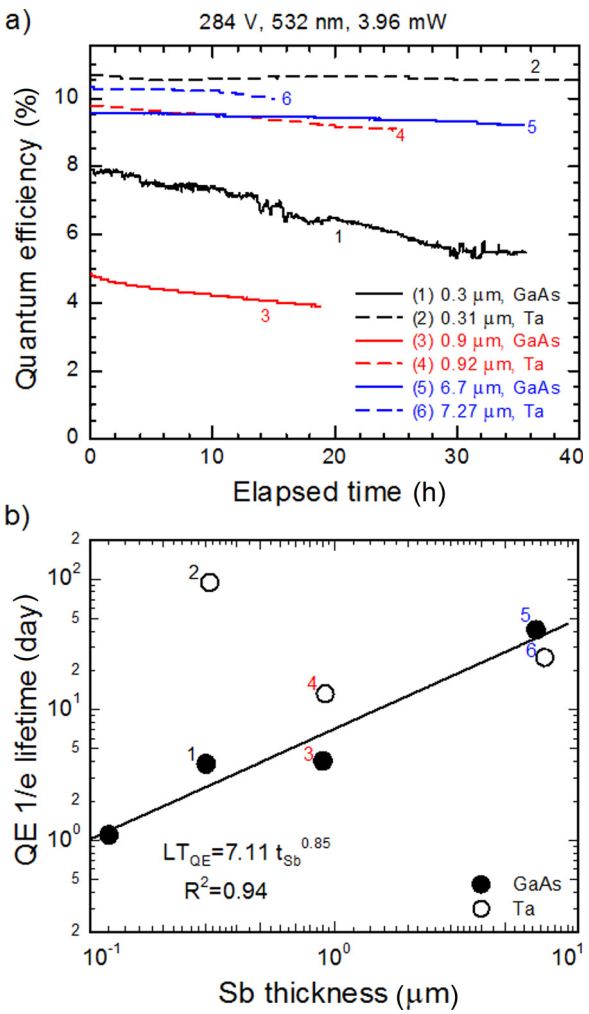

FIG. 9. (Color online) (a) QE decay as a function of illumination time, (b) QE lifetime as a function of Sb thickness (t_{Sb}) for bialkali-antimonide photocathodes created under vent-no bake practice. The photocathodes were prepared by bialkali codeposition following the vent-no bake protocol and illuminated with 532 nm (3.96 mW) at 284 V bias.

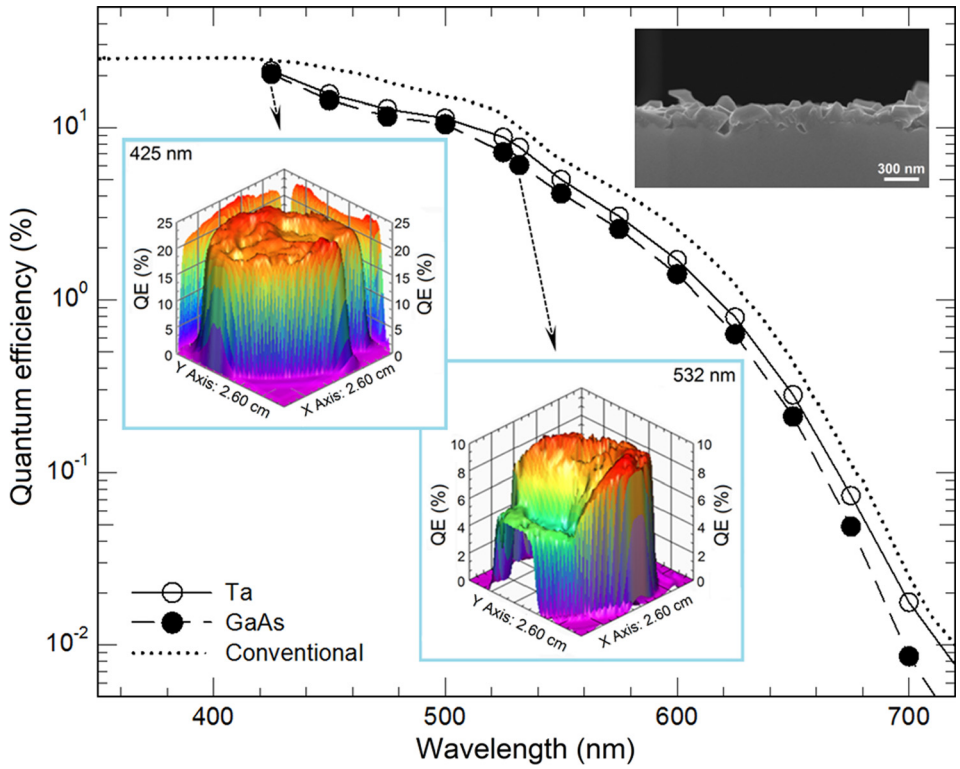

FIG. 10. (Color online) Spectral response of bialkali-antimonide photocathode deposited on Ta and GaAs substrates are shown together with the spectral response of conventional bialkali-antimonide photocathodes used in photomultiplier tubes. QE distribution is shown for 425 and 532 nm. The photocathode was prepared by bialkali codeposition on Sb layer of ~300 nm thickness deposition following the vent-no bake protocol.

after this 5 days period only when a brief illumination interruption was made. This brief interruption enabled the estimation of the QE 1/e lifetime in excess of 90 days. However, for thicker Sb layers, the observed lifetime followed a similar trend as those grown on the GaAs substrate.

D. Spectral response

The low power laser was replaced with the wavelength tunable light source to measure the QE as a function of wavelength from 425 to 825 nm [Fig. 10], for the photocathode with Sb layer of ~300 nm thickness (inset). For this photocathode, the highest QE from the Ta and GaAs substrates was 10% and 8% at 532 nm, and 24.2% and 22% at 425 nm, respectively. The QE distribution map at 532 nm depicted significant nonuniformity, which was due to an unintentional nonuniform chemical deposition. However, the effect of this spatial nonuniformity on QE distribution map appeared to minimize at 425 nm. This is likely because the effectiveness of light detection by a photocathode surface at different wavelength is known to depend on photocathode stoichiometry.[47] Any variation in photocathode stoichiometry is expected to accompany a variation in bandgap energy which will result in the light absorption edge to vary[48] and in turn it can influence the photoelectron transport to the surface.[49] Furthermore, the stoichiometry of alkali-antimonide photocathodes varies as a function of depth from the expected CsK_2Sb composition due to varying diffusion of the alkali materials in the underlying Sb layer.[50]

The obtained spectral response correlates well with the reference conventional curve[44] which represents a photocathode with very thin Sb layer (15 nm).[18] This indicates a good stoichiometry of our photocathodes with thick Sb layers grown by codeposition of alkalis.[51] The codeposition thus enabled optimal stoichiometry of photocathodes with very thick Sb layers.

E. Correlations between Sb thickness, chemical consumption, and photocathode optical performance

The relative amount of source materials required for each photocathode was estimated by noting the duration of deposition, the partial pressure of each chemical species as indicated by the RGA, and using the following formula:

$$Q = \frac{t \times P}{t_o \times P_o}, \tag{3}$$

where Q represents the normalized quantity of a particular chemical species relative to the Cs amount applied to the photocathode manufactured with the thinnest Sb layer (denoted by the index o); t represents the time duration of depositions; and P is the partial pressure detected by the RGA. Figure 11 exhibits a strong correlation between the chemical requirements and the Sb thickness. The Sb thickness and the required quantity of Cs and K increased exponentially with the applied amount of Sb. The required quantity of Cs and K also exhibited a power-law dependence on the Sb film thickness.

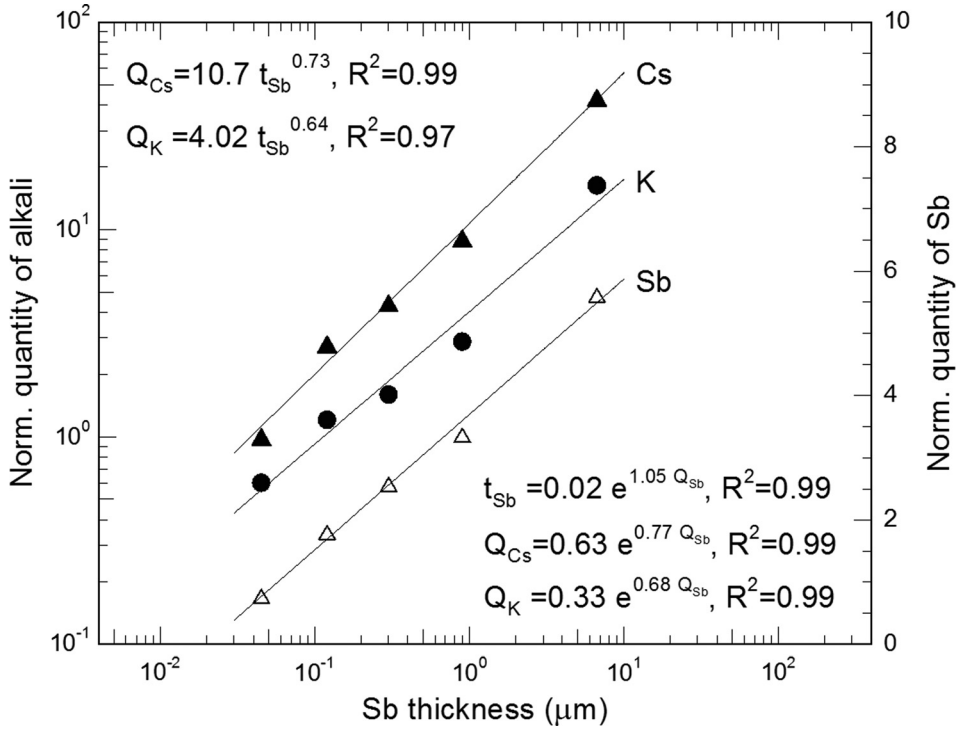

FIG. 11. Normalized quantity (Q) of source materials for optimal QE as a function of Sb thickness (t_{Sb}) for bialkali-antimonide photocathodes manufactured via codeposition of alkali species.

To explain some of the observations reported here, we speculate that photocathode performance using relatively thick Sb layers depends heavily on the surface morphology of the Sb film. In general, thin Sb films are smooth and dense compared to thicker Sb films that exhibit a high degree of roughness and porosity. Initially, the Sb films formed amorphous layers with discontinuous nucleation of grains. With further addition of Sb, the nucleation saturation occurred and a full surface coverage by Sb grains was obtained. The film subsequently grew increasingly thicker and exhibited larger grain structure with increased intergranular voids (Figs. 2, 4, and 5), which served to increase the total surface area of Sb grains. The required amount of alkali materials for optimum QE will depend on the ratio of the effective surface area to the volume of Sb. It is clear that thicker layers of Sb served to "store" more alkalis. The QE lifetime results shown in Fig. 9(b) indicated that photocathodes with more alkali storage provided longer lifetime in a manner similar to that of porous substrates used in a dispenser photocathodes,[52] which served as an alkali-reservoir.

The increase in lifetime with respect to an increase in Sb thickness can be attributed to the increasing ability of the photocathodes to replenish the depleted alkali species from the top surface over time. For Cs-based photocathodes, the QE decay can be attributed to the loss of Cs (Ref. 41) from the convoluted effect of electron induced gas desorption[53] or ion bombardment (in dc guns) and the susceptibility of surface coating to evaporation.[52] The probable other factor with minor influence on the QE lifetime is the effect of the seasoning of the wall of the chamber in terms of water partial pressure reduction during a series of activation. The alkali coating on the chamber structure acted as a getter for water which can poison a Cs based photocathode.[54,55] This observation supports the reported fact that the photocathode lifetimes usually increase when the region surrounding the photocathode becomes coated with Cs after successive activation.[56]

IV. CONCLUSION

Antimony films grown on Ta and GaAs substrates were studied under different vacuum and deposition conditions, to better understand growth characteristics and their effect on photocathode QE and lifetime at low voltage. A field emission scanning electron microscope was used to evaluate the Sb-layer morphology as a function of Sb-layer thickness and to correlate the latter with partial pressures registered by the RGA. This allowed us to use the RGA as a chemical deposition rate monitor. Thin Sb layers provided a relatively dense smooth surface, whereas thick Sb layers appeared porous with increased surface roughness. Vacuum conditions affected the growth of Sb differently on different substrates, but with degraded vacuum this difference was minimized. The Sb films grew easily into polycrystalline form. The grain enlargement, an increase in the surface roughness, and the crystallite size enlargement were associated with increasing Sb film thickness.

Subsequent to the Sb-film characterization, the bialkali-antimonide photocathodes were fabricated by codeposition of K and Cs by means of an effusion source onto the Sb films of varying thickness. The Ta and GaAs substrates with Sb films of comparable thickness showed similar QE from ~3% to 10% for photocathodes with Sb layer thickness ranging

from <50 nm to ~7 μm. A variation in the QE in the samples was attributed to the convoluted effect of structural variation, nonuniformity in chemical deposition, and substrate cleaning requirement that could affect the energy bandgap. We believe that the codeposition supported the formation of QE-optimized photocathodes when thick Sb layers were used, compared to those manufactured using sequential deposition. The performance of photocathodes was correlated with the Sb thickness and alkali consumption, where porous and thick Sb layers exhibited the best lifetime at low-voltage. The high-capacity effusion source enabled us to successfully manufacture alkali-antimonide photocathodes having maximum QE ~10% and extended low voltage lifetime (>90 days) at 532 nm. We speculate that the Sb layer served as a reservoir, or sponge, for the alkali materials in the bialkali-antimonide photocathodes. Photocathodes such as these will be tested inside a dc high voltage photogun in future, where we expect to correlate some of the observations reported here, with measurements of photocathode lifetime at high voltage and beam quality including beam emittance.

One of the frequently asked questions related to bialkali-antimonide photocathodes is whether some amount of contamination in CsK_2Sb serves a beneficial role[31] in the chemical processes that govern bialkali-antimonide photocathode formation. This work illustrates that strict vacuum protocols (i.e., baking) are not absolutely essential, but it does not specify limits on the partial pressure of different gas species, including water vapor. A worthy follow up study could explore the impact of different gas species on bialkali-antimonide photocathode formation, with gas species like water vapor, introduced into the vacuum chamber in a more controlled manner.

ACKNOWLEDGMENTS

This material is based on work supported by the U.S. Department of Energy, Division of Material Sciences, under Grant No. DE-FG02-97ER45625, and the National Science Foundation Grant No. DMR-0420304. The authors thank Kai Zhang of ODU and the College of William & Mary for the use of FESEM to obtain the microscopic images.

[1]D. Dowell *et al.*, Nucl. Instrum. Method A **622**, 685 (2010).
[2]R. R. Mammei *et al.*, Phys. Rev. Spec. Top.-Accel. **16**, 033401 (2013).
[3]D. H. Dowell, S. Z. Bethel, and K. D. Friddell, Nucl. Instrum. Method A **356**, 167 (1995).
[4]R. Mirzoyan, M. Laatiaoui, and M. Teshima, Nucl. Instrum. Method A **567**, 230 (2006).
[5]L. Cultrera *et al.*, Phys. Rev. Spec. Top.-Accel. **14**, 120101 (2011).
[6]S. H. Kong, J. Kinross-Wright, D. C. Nguyen, and R. L. Sheffield, Nucl. Instrum. Method A **358**, 272 (1995).
[7]T. Vecchione, I. Ben-Zvi, D. H. Dowell, J. Feng, T. Rao, J. Smedley, W. Wan, and H. A. Padmore, Appl. Phys. Lett. **99**, 034103 (2011).
[8]L. Cultrera *et al.*, Proceedings of IPAC2012, New Orleans, Louisiana, WEOAB02 (2012), p. 2137; https://accelconf.web.cern.ch/accelconf/IPAC2012/papers/weoab02.pdf.
[9]R. Huang, D. Filippetto, C. F. Papadopoulos, H. Qian, F. Sannibale, and M. Zolotorev, Phys. Rev. Spec. Top.-Accel. **18**, 013401 (2015).
[10]A. Bartnik *et al.*, *Cornell ERL: Project Definition Design Report*, edited by G. H. Hoffstaetter, S. M. Gruner, and M. Tigner (Cornell University, New York, 2013); http://www.classe.cornell.edu/rsrc/Home/Research/ERL/PDDR/PDDR.pdf.
[11]"Linac coherent light source II conceptual design report," https://portal.slac.stanford.edu/sites/lcls_public/lcls_ii/Published_Documents/CDR%20Index.pdf.
[12]J. Balewski *et al.*, "DarkLight: A search for dark forces at the Jefferson Laboratory free-electron laser facility," e-print arXiv:1307.4432v2 [physics.ins-det].
[13]A. W. Thomas, "An electron-ion collider at Jefferson lab," e-print arXiv:0907.4785v1 [hep-ex].
[14]V. Ptitsyn *et al.*, *Proceedings of EPAC 2004*, Lucerne, Switzerland (2004), p. 923; https://www.bnl.gov/isd/documents/28582.pdf.
[15]C. K. Sinclair *et al.*, Phys. Rev. Spec. Top.-Accel. **10**, 023501 (2007).
[16]W. von. Drachenfels, F. Frommberger, M. Gowin, W. Hillert, M. Hoffmann, and B. Neff, AIP Conf. Proc. **675**, 1053 (2003).
[17]S. Benson *et al.*, Nucl. Instrum. Method A **582**, 14 (2007).
[18]J. Smedley *et al.*, *Proceedings of PAC2013*, Pasadena, California, USA, THPAC17 (2013), p.1178; http://accelconf.web.cern.ch/accelconf/pac2013/papers/thpac17.pdf.
[19]D. E. Persyk, J. Morales, R. McKeighen, and G. Muehllehner, IEEE Trans. Nucl. Sci. **26**, 364 (1979).
[20]G. A. Condas and F. O. Wooten, J. Appl. Phys. **32**, 323 (1961).
[21]H. Levinstein, J. Appl. Phys. **20**, 306 (1949).
[22]M. Hashimoto, H. Sugibuchi, and K. Kambe, Thin Solid Films **98**, 197 (1982).
[23]N. Kaiser, Thin Solid Films **116**, 259 (1984).
[24]D. M. Dunham and C. K. Sinclair, "Charging the cesiator on the Illinois/CEBAF polarized electron source," NPL Polarized source Group Technical Note No. 90-9 (Nuclear Physics Laboratory, University of Illinois at Urbana-Champaign, IL, 1990).
[25]C. Y. Prescott *et al.*, Phys. Lett. B **77**, 347 (1978).
[26]M. A. Mamun, C. Hernandez-Garcia, M. Poelker, and A. A. Elmustafa, APL Mater. **3**, 066103 (2015).
[27]Micro Model 8790-00 liquid cleaner, Cole-Parmer Instrument Company, Detergent ultrasonic cleaning was followed by solvent rinses in acetone and methanol, then a rinse in DI water.
[28]Alkali Metal Dispensers Brochure 1789, SAES getters, 20020 Lainate (MI) Italy (2007).
[29]W. E. Spicer and A. Herra-Gomez, "Modern theory and applications of photocathodes," SLAC-PUB-6306, August 1993, paper presented at the SPIE's 1993 International symposium on optics, imaging and instrumentation, San Diego, CA, USA, 11–16 July 1993.
[30]M. Succi, R. Canino, and B. Ferrario, Vacuum **35**, 579 (1985).
[31]B. M. van Oerle and G. J. Ernst, Nucl. Instrum. Method A **358**, 287 (1995).
[32]K. L. Jensen, D. W. Feldman, N. A. Moody, and P. G. O'Shea, J. Appl. Phys. **99**, 124905 (2006).
[33]NKT Photonics, "SuperK EXTREME supercontinuum lasers," http://www.nktphotonics.com/superkextreme.
[34]ICDD PDF Card No.: 01-085-1322.
[35]ICDD PDF Card No.: 01-077-3388.
[36]X. Liang *et al.*, *Proceedings of PAC2013*, Pasadena, California, USA, THPAC12 (2013), p.1163; http://accelconf.web.cern.ch/AccelConf/pac2013/papers/thpac12.pdf.
[37]B. D. Cullity and S. R. Stock, *Elements of X-ray Diffraction*, 3rd ed. (Prentice-Hall, NJ, 2001), p. 167.
[38]K. L. Lopez-Maldonado, P. de la Presa, M. A. de la Rubia, P. Crespo, J. deFrutos, A. Hernando, J. A. M. Aquino, and J. T. E. Galindo, J. Nanopart. Res. **16**, 2482 (2014).
[39]K. L. Chopra, *Thin Film Phenomena* (McGraw-Hill, New York, 1969).
[40]A. Braem, C. Joram, F. Piuz, E. Schyns, and J. Séguinot, Nucl. Instrum. Method A **502**, 205 (2003).
[41]A. H. Sommer, *Photoemissive Materials* (Wiley, New York, 1968).
[42]K. Nakamura, Y. Hamana, Y. Ishigami, and T. Matsui, Nucl. Instrum. Method A **623**, 276 (2010).
[43]V. P. Geetha Vani, M. Vasudeva Reddy, and K. T. Ramakrishna Reddy, ISRN Condens. Matter Phys. **2013**, 142029.
[44]M. Suyama, *Proceedings of Science*, Kobe, Japan, PD07 (2007), p. 018.
[45]M. Ruiz-Osés *et al.*, APL Mater. **2**, 121101 (2014).
[46]D.-A. Luh *et al.*, "Recent polarized photocathode R&D at SLAC," AIP Conf. Proc. **675**, 1029 (2003).
[47]G. S. Buller and R. J. Collins, Meas. Sci. Technol. **21**, 012002 (2010).
[48]M. A. Khan and R. G. Schulze, U.S. patent 4616248 (7 October 1986).

[49]"Development of high quantum efficiency UV/blue photocathode epitaxial semiconductor heterostructures for scintillation and Cherenkov radiation detection," Summary of Research, PI: Daniel J. Leopold, 7-15-200 to 7-14-2002, Washington University, NASA Grant No.: NAG5-8536.
[50]L. Xu-Dong, G. Qiang, Z. Meng, and Z. Ming-Hua, Chin. Phys. C **36**, 531 (2012).
[51]P. Michelato, Nucl. Instrum. Method A **393**, 455 (1997).
[52]E. J. Montgomery, D. W. Feldman, P. G. O'Shea, Z. Pan, N. Sennett, K. L. Jensen, and N. A. Moody, J. Directed Energy **3**, 66 (2008); http://www.ipr.umd.edu/sites/default/files/documents/Montgomery-Eric-MS-2009.pdf.
[53]D. Schultz *et al.*, "The high peak current polarized electron source of the Stanford Linear Collider," SLAC-PUB-6275, June 1993, paper presented at the workshop on high intensity electron sources, Legnaro, Padua, Italy, 24–28 May 1993; http://inspirehep.net/record/356246/files/slac-pub-6275.pdf.
[54]D. Durek, F. Frommberger, T. Reichelt, and M. Westermann, Appl. Surf. Sci. **143**, 319 (1999).
[55]T. Wada, T. Nitta, T. Nomura, M. Miyao, and M. Hagino, Jpn. J. Appl. Phys.**29**, 2087 (1990).
[56]*Atomic, Molecular: Optical Physics: Charged Particles*, Experimental Methods in the Physical Sciences, edited by F. B. Dunning and R. G. Hulet (Academic, San Diego, CA, 1998), Vol **29A**, p. 22.